Journal of Catalysis 311 (2014) 393–403

Contents lists available at ScienceDirect

Journal of Catalysis

journal homepage: www.elsevier.com/locate/jcat

Doping effects of B in ZrO_2 on structural and catalytic properties of Ru/B-ZrO_2 catalysts for benzene partial hydrogenation

Gongbing Zhou [a], Yan Pei [a], Zheng Jiang [b], Kangnian Fan [a], Minghua Qiao [a,*], Bin Sun [c], Baoning Zong [c,*]

[a] Department of Chemistry and Shanghai Key Laboratory of Molecular Catalysis and Innovative Materials, Fudan University, Shanghai 200433, PR China
[b] Shanghai Synchrotron Radiation Facility, Shanghai Institute of Applied Physics, Chinese Academy of Sciences, Shanghai 201204, PR China
[c] The State Key Laboratory of Catalytic Materials and Reaction Engineering, Research Institute of Petroleum Processing, Beijing 100083, PR China

ARTICLE INFO

Article history:
Received 9 October 2013
Revised 27 December 2013
Accepted 31 December 2013
Available online 31 January 2014

Keywords:
B dopant
ZrO_2
Lewis acidity
Ru
Benzene
Hydrogenation
Cyclohexene

ABSTRACT

The B-doped ZrO_2 (B-ZrO_2) samples with different B/Zr ratios were synthesized using zirconium oxychloride and boric acid as the precursors. Their crystallographic phase retained as tetragonal ZrO_2 after the doping of B; however, the amount of the Lewis acid sites increased from 46.1 $\mu mol_{NH3}\, g^{-1}$ on ZrO_2 to 100.6 $\mu mol_{NH3}\, g^{-1}$ on B-ZrO_2(1/10) with the nominal B/Zr molar ratio of 1/10. The Ru/B-ZrO_2 catalysts were then prepared by chemical reduction, and their electronic and structural properties were systematically characterized by spectroscopic techniques. It is identified that the Ru nanoparticles (NPs) supported on these B-ZrO_2 samples exhibited similar size, chemical state, and microstructure. In the partial hydrogenation of benzene, the turnover frequency of benzene was linearly proportional to the amount of the acid sites on the supports, whereas the selectivity toward cyclohexene displayed a volcanic evolution passing through a maximum of 88% on the Ru/B-ZrO_2(1/15) catalyst. Kinetic analysis indicated that the acid sites improved the rate constants of the benzene to cyclohexene step (k_1) and the cyclohexene to cyclohexane step (k_2) to different degrees. The resulting k_1/k_2 ratio increased from $3.7 \times 10^{-2}\, l\, mol^{-1}$ (Ru/ZrO_2) to $4.8 \times 10^{-2}\, l\, mol^{-1}$ (Ru/B-ZrO_2(1/15)), and then declined to $4.1 \times 10^{-2}\, l\, mol^{-1}$ (Ru/B-ZrO_2(1/10)), which explained the volcanic evolution of the selectivity toward cyclohexene with respect to the acid amount.

1. Introduction

Cyclohexene is an important chemical as its reactive C=C bond facilitates facile conversion to value-added cyclohexanol, caprolactam, and adipic acid via typical olefin reactions. The production of cyclohexene by benzene partial hydrogenation features exceptional superiority to processes including dehydration of cyclohexanol, dehydrogenation of cyclohexane, and the Birch reduction in terms of inexpensive feedstock, succinct reaction route, and consequently, operational simplicity [1]. However, it remains a great challenge to achieve a high yield of cyclohexene from benzene owing to severe thermodynamic limitation. The standard free energy change for cyclohexene formation from benzene hydrogenation ($-23\ kJ\ mol^{-1}$) is much less negative than that for cyclohexane formation ($-98\ kJ\ mol^{-1}$) [2]. Therefore, the development of a highly effective catalyst that is capable of steering the product to cyclohexene has been intensively pursued not only for its fundamental interest, but also for its industrial significance [3,7].

Despite the wide acceptance of the stepwise hydrogenation mechanism of benzene (benzene to cyclohexene followed by cyclohexene to cyclohexane) [6,8], the roles of the catalyst components in the partial hydrogenation of benzene, such as the surface acid sites of the supports, remain obscure. Several reviews claimed that benzene hydrogenation was a purely metal-catalyzed reaction [9,10], while many works demonstrated that the support acidity imposed remarkable effect on the activity of the supported metal catalysts [11–14]. de Mallman and Barthomeuf found that the rate of benzene hydrogenation increased with the concentration of the acid sites on Pt–faujasites [11]. Wang et al. proposed that the presence of additional hydrogenation sites at the metal–acid interface underlay the activity enhancement of benzene hydrogenation on the Pt/Al-MCM-41 catalyst with stronger acidity [12]. Lercher and coworkers put forward a detailed reaction pathway of benzene hydrogenation involving the Brønsted acid sites [13]. They identified that benzene hydrogenation on Pt/mordenites took place along two parallel reaction pathways, i.e., hydrogenation (i) on the metal surface and (ii) on the acid sites in the vicinity of Pt particles with hydrogen dissociated on the metal. The latter reaction pathway depends on the concentration of Brønsted acid sites of the zeolite and on the metal and acid site vicinity [13]. Benzene hydrogenation has also been suggested to occur on the Lewis acid

* Corresponding authors. Fax: +86 21 65641740 (M. Qiao), +86 10 82368011 (B. Zong).
E-mail addresses: mhqiao@fudan.edu.cn (M. Qiao), zongbn.ripp@sinopec.com (B. Zong).

0021-9517/$ - see front matter © 2014 Elsevier Inc. All rights reserved.
http://dx.doi.org/10.1016/j.jcat.2013.12.022

sites of the support [14]. The Lewis acid site is an electron-deficient center, whereas benzene with the delocalized π bonds tends to be an electron donor. On the Pt/γ-Al_2O_3 and Pt/HAl-MCM-41 catalysts with the supports having the Lewis acid sites, benzene could be adsorbed easily on the Lewis acid sites with the formation of electron-deficient aromatic intermediates, which can be hydrogenated by activated hydrogen atoms [14]. Lin and Vannice found that the intrinsic activity increased in the order of Pt/η-Al_2O_3 < Pt/SiO_2 < Pt/SiO_2·Al_2O_3 < Pt/TiO_2 with the same order of the acid amounts on the supports in benzene hydrogenation [15], which was attributed to the occurrence of additional hydrogenation of benzene adsorbed on the acid sites of the support with spillover hydrogen (H_{so}).

ZrO_2 is an important catalyst support in benzene partial hydrogenation [16,17]. Previous works have demonstrated that the acidic property of ZrO_2 can be adjusted by B_2O_3 [18]. In this connection, herein we synthesized a series of B-doped ZrO_2 (B-ZrO_2) with different doping levels of B with the aim to tailor the acidic property of ZrO_2. With these well-characterized B-ZrO_2 supports, the Ru/B-ZrO_2 catalysts were prepared by the wetness impregnation–chemical reduction method. The influences of the doping level of B on the textural, electronic, and structural properties of the Ru/B-ZrO_2 catalysts were investigated in detail. Correlation of the physicochemical properties of the Ru/B-ZrO_2 catalysts with the catalytic performances in the partial hydrogenation of benzene to cyclohexene was attempted. The relationships between the amounts of the Lewis acid sites on the catalytic activity and the selectivity toward cyclohexene were unveiled and discussed.

2. Experimental

2.1. Preparation

The chemicals, if unspecified, were of analytical grade (A.R.) and purchased from Sinopharm Chemical Reagent. The gases were purchased from Shanghai Youjiali Liquid Helium. The B-doped ZrO_2 samples were synthesized according to Urbano et al. with some modifications [18]. Namely, the ammonia solution (25–28 wt%) was added dropwise to a mixed aqueous solution of $ZrOCl_2·8H_2O$ (0.5 M) and H_3BO_3 to the pH of 10 under vigorous stirring at room temperature, and then refluxed at 373 K for 24 h. The precipitates were separated by centrifugation, reslurried and washed thoroughly with deionized water until the pH of 7 and the removal of the chloride ions ($AgNO_3$ test), dried at 373 K in air for 24 h, and calcined in air at 1073 K for 5 h at a heating rate of 10 K min^{-1}. The nominal B/Zr molar ratios were 1/20, 1/15, and 1/10. The B-doped ZrO_2 was labeled B-ZrO_2(x), where x represents the nominal B/Zr ratio. Pure ZrO_2 was prepared following the same procedures described above but in the absence of H_3BO_3.

The Ru/B-ZrO_2 catalysts were prepared by wetness impregnation, followed by chemical reduction. Specifically, exactly one gram of the B-ZrO_2 sample was impregnated with 30 ml of 26.4 mM aqueous solution of $RuCl_3·3H_2O$ (A.R., Shanghai Aoke) and stirred for 48 h at room temperature. The theoretical Ru loading was 7.4 wt% for all the catalysts. Then, 2.0 ml of the 1.58 M aqueous solution of KBH_4 was added dropwise to the slurry at room temperature under mild stirring. The molar ratio between KBH_4 and Ru^{3+} was 4/1. The black solids were washed thoroughly with deionized water until all the chloride ions were removed ($AgNO_3$ test). Surface analysis confirmed that there was no residual Cl on the catalyst surface. The obtained catalyst was denoted as Ru/B-ZrO_2(x).

2.2. Characterization

The multipoint Brunauer–Emmett–Teller surface area (S_{BET}) was measured by N_2 physisorption at 77 K on a Micromeritics TriStar3000 apparatus. The sample was loaded in a glass adsorption tube and pretreated at 523 K under flowing N_2 for 5 h. The bulk composition was determined by the inductively coupled plasma-atomic emission spectroscopy (ICP–AES; Thermo Elemental IRIS Intrepid). Powder X-ray diffraction (XRD) pattern was acquired on a Bruker AXS D8 Advance X-ray diffractometer using Ni-filtered Cu Kα radiation (λ = 0.15418 nm). The tube voltage was 40 kV, and the current was 40 mA. The 2θ angles were scanned from 20° to 70° at 4° min^{-1}.

The nature of the acid site was characterized by the FTIR spectroscopy of adsorbed pyridine (Py-IR) on a Nicolet Nexus 470 spectrometer equipped with a DTGS detector and a temperature-control accessory to provide sequences of the temperature-dependent spectra. About 15 mg of the sample was pressed with KBr into a self-supporting wafer of 2 cm in diameter. The wafer was placed in an IR cell with CaF_2 windows, evacuated at 473 K for 4 h, and then cooled to 298 K. After the background spectrum was recorded, pyridine was introduced and balanced at this temperature for 1 h. Physisorbed pyridine was removed by evacuation at 298 K. Then, the sample was heated under vacuum to 373 K, at which the spectrum was recorded with 4 cm^{-1} resolution by signal-averaging 32 scans. The amount of the Lewis acid sites involved in adsorbing pyridine (n_{Py}) was estimated by the method proposed by Hughes and White firstly on the basis of the integrated Lambert–Beer law [19] and then transformed by Onfroy et al. to the form of $n = SA/m\varepsilon$ [20]. In this equation, S, A, m, and ε are the surface area of the wafer, the integral absorption band intensity of the Lewis acid sites-bonded pyridine (L-Py), the weight of the sample, and the integral extinction coefficient, respectively. According to Onfroy et al. [20], the ε value varied little with the types of the solids. Thus, the ε value of 2.4 cm μmol^{-1} determined by Travert et al. for the 1459 cm^{-1} band of the L-Py on the B_2O_3–SiO_2 oxides at 373 K [21] was adopted in the calculation of the n_{Py}.

NH_3-TPD was carried out on a Micromeritics 2750 chemisorption system. The weighed sample (~150 mg) was pretreated at 473 K for 1 h under He and cooled to 393 K. The 10 vol% NH_3/He mixed gas was introduced instead of He at this temperature for 1 h to ensure the saturation adsorption of NH_3 [22]. The sample was then purged with He until the signal returned to the baseline as monitored by a thermal conductivity detector (TCD). The desorption curve of NH_3 was acquired by heating the sample from 393 K to 993 K at 10 K min^{-1} under He with the flow rate of 25 ml min^{-1}. Comparison of the area of the desorption peak with that calibrated by a 500 μl-capacity loop allowed for quantifying the total amount of the acid sites per gram of the sample.

CO chemisorption was used to determine the dispersion and active surface area (S_{Ru}) of Ru, which was also performed on the Micromeritics 2750 chemisorption system. The weighed sample (~100 mg) was pretreated at 473 K for 1 h under He and cooled to 298 K. Pure CO pulses were injected until the eluted peak did not change in intensity [23]. The dispersion of Ru and S_{Ru} was calculated according to the CO uptake with the assumptions of the CO:Ru stoichiometry of 0.5:1 [24] and the Ru surface atomic density of 1.63×10^{19} atoms m^{-2} [22].

X-ray photoelectron spectroscopic (XPS) spectrum was collected on a Perkin-Elmer PHI5000C instrument with Mg Kα radiation ($h\nu$ = 1253.6 eV) as the excitation source. The catalyst protected by ethanol was mounted on the sample plate, degassed in the pretreatment chamber in vacuo at 298 K overnight, and then transferred to the analyzing chamber where the background pressure was lower than 2×10^{-9} Torr. As the Ru 3d peak partly overlapped with the C 1s peak of the contaminant carbon, all binding energy (BE) values were referenced to the Zr $3d_{5/2}$ BE of ZrO_2 at 182.2 eV with an uncertainty of ±0.2 eV.

The surface morphology, particle size, and the selected-area electron diffraction (SAED) pattern were observed by transmission

electron microscopy (TEM) on a JEOL JEM2011 microscope operated at 200 kV, which was coupled with an energy-dispersive X-ray analyzer (EDX; Oxford INCA) for local elemental determination. The catalyst was dispersed in anhydrous ethanol, sonicated for 10 min, and dropped onto a carbon film-coated copper grid. Particle size distribution (PSD) histogram was constructed by randomly measuring at least 300 NPs.

X-ray absorption spectrum at the Ru K-edge was acquired on the BL14W1 beamline of the Shanghai Synchrotron Radiation Facility (SSRF) in the fluorescence mode. The typical electron beam energy was 3.5 GeV, and the current was 300 mA. The catalyst was coated on the scotch tape, pressed into the Al window, and inserted in the sample stage. X-ray absorption near-edge structure (XANES) was compared after normalization. Extended X-ray absorption fine structure (EXAFS) data were analyzed by the IFEFFIT analysis package following the standard procedures [25]. The background was removed by extrapolating the pre-edge region onto the EXAFS region, and the $\chi(E)$ data were normalized with respect to the edge jump step using the Athena program of the IFEFFIT package [26]. The normalized $\chi(E)$ was transformed from the energy space to the k-space with the $\chi(k)$ multiplied by k^2 to compensate for the oscillations in the high-k region. Then, the k^2-weighted $\chi(k)$ data in the k-space ranging from 3.2 to 11.4 Å^{-1} (for the Ru foil standard, 3.2–14.0 Å^{-1}) were Fourier transformed to the R-space. The processed $\chi(k)$ data were fitted in the R-space ranging from 0.2 to 2.8 Å (for the Ru foil, 0.8–2.8 Å) using the Artemis program of the IFEFFIT package [26]. For disordered systems, the symmetric Gaussian pair distribution function is invalid for the nearest neighbor atom distribution, so we carried out the Gaussian approximation fitting procedure with third order cumulant representing the big disorder in the structure [27]. From these analyses, structural parameters, such as coordination number (N), coordination distance (R), Debye–Waller factor ($\Delta\sigma^2$), and inner potential correction (ΔE_0), were obtained.

Diffuse reflectance infrared Fourier transform spectroscopy (DRIFTS) of hydrogen adsorbed on the catalysts was performed on a Nicolet 6700 spectrometer with a DTGS detector with 4 cm^{-1} resolution by signal-averaging 32 scans. Five milligrams of the catalyst dried in He flow at 373 K was ground with 100 mg of KBr, and then about 15 mg of the mixed sample was transferred into an in situ IR cell under the protection of He. The sample was pretreated at 473 K for 1 h under He. After cooling to 293 K and recording the background spectrum, H_2 was introduced to replace He. The flow rate and pressure of He or H_2 are 20 ml min^{-1} and 0.1 MPa, respectively. Then, the sample was heated stepwise in the presence of H_2 from 293 to 413 K at a heating rate of 5 K min^{-1}. The spectra were recorded at 323, 353, 383, and 413 K after balancing at each temperature for 30 min.

The adsorption capacity of benzene on the catalyst was examined by temperature-programed desorption (TPD) on a thermogravimetric analyzer (TA Instruments SDT-Q600) attached to a Pfeiffer Instruments GSD 301 T2 mass spectrometer (MS). The amount of the catalyst used in the test was about 25 mg. The catalyst was immersed in benzene for saturation adsorption, followed by drying at room temperature overnight under N_2. The MS spectrum was obtained at a heating rate of 10 K min^{-1} from 303 to 1073 K under N_2 with the flow rate of 40 ml min^{-1} by tracking the parent ion at the mass to charge ratio (m/z) of 78.

2.3. Catalytic testing

Up to now, methods for benzene partial hydrogenation can be categorized into batchwise liquid-phase [3–7] and continuous gas-phase modes [28]. The main advantage of the former is that it can achieve a much higher selectivity toward cyclohexene at high conversion level of benzene [3–7]. The partial hydrogenation of benzene was carried out in a mechanically stirred 500 ml-capacity stainless steel autoclave under conditions typical for this reaction [22,29]. The autoclave was charged with 100 ml of deionized water containing 1.0 g of the catalyst, 2.0 g of $ZnSO_4{\cdot}7H_2O$, 50 ml of benzene, and then sealed and purged with H_2 for four times to expel air. It was proposed that water renders a stagnant water layer surrounding the catalyst, resulting in the suppression of the reaction rate and in a strong increase in the selectivity and yield of cyclohexene [30]. $ZnSO_4{\cdot}7H_2O$ is the most effective modifier in improving the selectivity toward cyclohexene [31–33] among abundant additives investigated such as NaOH [3], ethanolamine [5], PEG-10000 [34], monoethanolamine [35], and monoethyleneglycol [35]. For benzene partial hydrogenation to cyclohexene, water and $ZnSO_4$ are indispensable for obtaining an appreciable selectivity toward cyclohexene. Otherwise, cyclohexane, the complete hydrogenation product, will dominate throughout the reaction course, with no or trace cyclohexene being harvested. The reaction conditions were 413 K, the overall pressure of 4.0 MPa, and the stirring rate of 1000 rpm, which is sufficient to eliminate the diffusion effect [29]. The reaction conditions employed herein are typical in the literature for benzene partial hydrogenation [3,6–8]. The reaction course was monitored by discharging ~0.3 ml of the reaction mixture at intervals, followed by analysis on a GC122 gas chromatograph fitted with a PEG-20 M packed column and a TCD. The catalytic performances of the catalysts were evaluated at least in duplicate, and results from replicate runs agreed to within ±2%. The catalytic activity was expressed as the weight-specific activity (r_0) and, further, as the TOF of benzene. The former was the amount of benzene converted per minute per gram of the catalyst at zero reaction time, which was obtained by procedures proposed by Hu and Chen [7]. The experimental benzene content–reaction time (t) curve was fitted by a polynomial equation, which was then differentiated, and the r_0 was acquired by substituting zero for t. The latter was expressed as TOF = $r_0 \times M_{Ru}/(\text{dispersion} \times W)$, in which M_{Ru} and W are the molar mass of Ru and the loading of Ru on the catalyst, respectively, and the dispersion of Ru is based on CO chemisorption. Because benzene cannot be hydrogenated on the ZrO_2 and B-ZrO_2 supports alone, Ru is undoubtedly the primary active site for this reaction. So, it is more suitable to use the Ru site to calculate the TOF as a good approximation. In heterogeneous catalysis, though it is very difficult to define exactly the nature of the active sites, comparing the TOFs on the same basis is advantageous for researchers to disclose and interpret activity difference between different catalysts [36]. The initial selectivity toward cyclohexene (S_0) was obtained by extrapolating the fitted selectivity–time curve of cyclohexene to zero reaction time, with the intercept being S_0.

3. Results and discussion

3.1. Composition, texture, and bulk structure of the B-ZrO_2 samples

Table 1 lists the compositional and textural properties of the ZrO_2 and the B-doped ZrO_2 samples. The practical B/Zr molar ratios increased monotonically with the nominal B/Zr ratios. However, only about one-third of the prescribed amounts of B were doped into ZrO_2. A similar phenomenon was observed by Urbano et al. on their B-ZrO_2 samples [18]. It is possible that the precipitation condition for Zr is not the optimal precipitation condition for B. The N_2 adsorption–desorption isotherms of the samples (Fig. S1) all belonged to type IV with H3 hysteresis loop. According to Table 1, the S_{BET} and the pore volume (V_{pore}) decreased while the average pore diameter (d_{pore}) increased accompanying the improvement of the doping level of B. The S_{BET} of the present ZrO_2 sample is higher than the value reported by Chuah et al.

Table 1
The physicochemical properties of the ZrO_2 and B-ZrO_2 samples.

Sample	B/Zr[a] (molar ratio)	S_{BET} ($m^2\ g^{-1}$)	V_{pore} ($cm^3\ g^{-1}$)	d_{pore} (nm)
ZrO_2	n.a.[b]	78	0.27	10.9
B-ZrO_2(1/20)	1/60	56	0.22	11.8
B-ZrO_2(1/15)	1/44	50	0.20	11.8
B-ZrO_2(1/10)	1/36	36	0.18	14.4

[a] Determined by ICP-AES.
[b] n.a.: Not applicable.

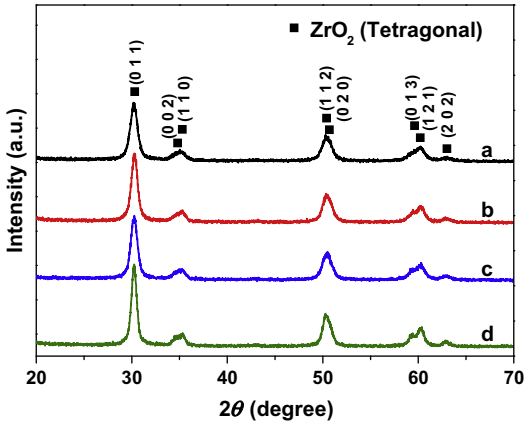

Fig. 1. XRD patterns of the (a) ZrO_2, (b) B-ZrO_2(1/20), (c) B-ZrO_2(1/15), and (d) B-ZrO_2(1/10) samples.

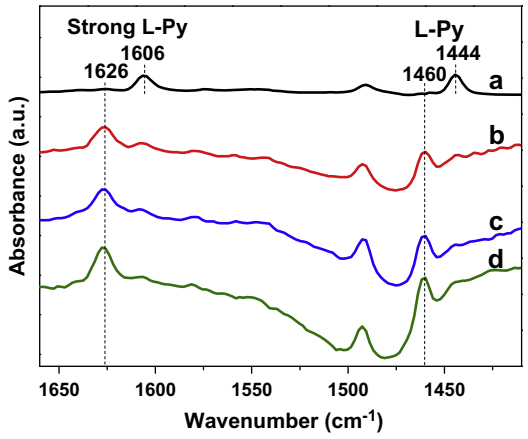

Fig. 2. Py-IR spectra of the (a) ZrO_2, (b) B-ZrO_2(1/20), (c) B-ZrO_2(1/15), and (d) B-ZrO_2(1/10) samples at 373 K.

Table 2
The acidic properties of the ZrO_2 and B-ZrO_2 samples.

Sample	A[a] (cm^{-1})	n_{Py}[b] ($\mu mol\ g^{-1}$)	n_{NH3}[c] ($\mu mol\ g^{-1}$)
ZrO_2	9.8	12.8	46.1
B-ZrO_2(1/20)	14.6	19.1	64.5
B-ZrO_2(1/15)	19.2	25.1	87.2
B-ZrO_2(1/10)	25.2	33.0	100.6

[a] The total integral absorption band intensity of L-Py at 1460 and 1444 cm^{-1} in the Py-IR spectra collected at 373 K.
[b] The amount of adsorbed pyridine determined by Py-IR.
[c] The amount of desorbed NH_3 determined by NH_3-TPD.

[37]. And the descending S_{BET} of ZrO_2 after B doping is consistent with the observation by Urbano et al. using the same Zr precursor but various B precursors [18].

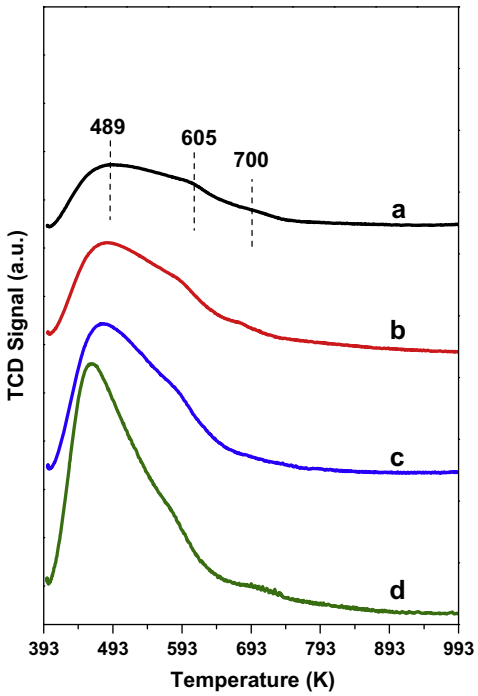

Fig. 3. NH_3-TPD profiles of the (a) ZrO_2, (b) B-ZrO_2(1/20), (c) B-ZrO_2(1/15), and (d) B-ZrO_2(1/10) samples.

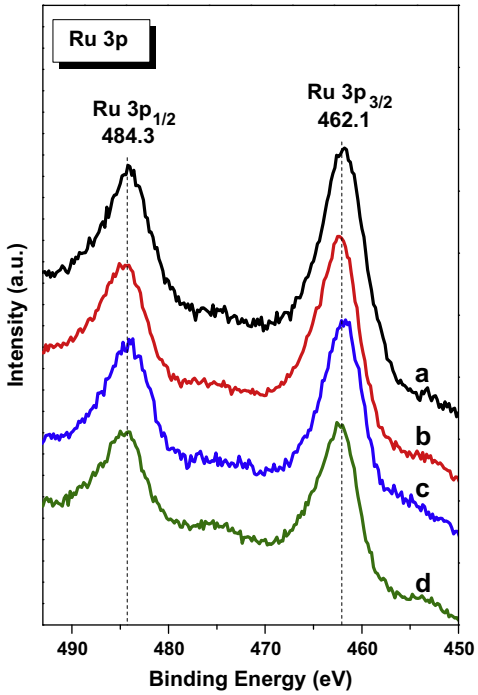

Fig. 4. Ru 3p XPS spectra of the (a) Ru/ZrO_2, (b) Ru/B-ZrO_2(1/20), (c) Ru/B-ZrO_2(1/15), and (d) Ru/B-ZrO_2(1/10) catalysts.

Fig. 1 shows the XRD patterns of the ZrO_2 and the B-doped ZrO_2 samples. The peaks at 2θ of 30.3°, 34.8°, 35.3°, 50.4°, 50.7°, 59.6°, 60.2°, and 63.0° for the ZrO_2 sample are readily assigned to tetragonal ZrO_2 (t-ZrO_2) (JCPDS 50-1089). The formation of an exclusive tetragonal phase is consistent with the work by Chuah et al. [37]. Our preparation procedures were similar to those of Chuah et al., with the Zr precursor being $ZrOCl_2$ of ours and $ZrCl_4$ of theirs. On

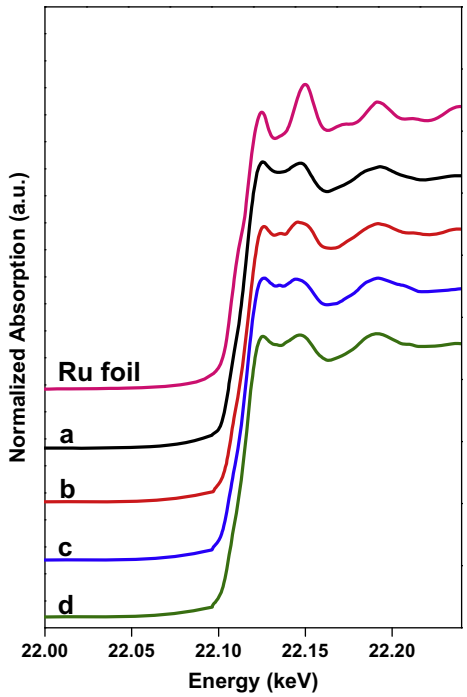

Fig. 5. Normalized Ru K-edge XANES spectra of the (a) Ru/ZrO_2, (b) $Ru/B\text{-}ZrO_2(1/20)$, (c) $Ru/B\text{-}ZrO_2(1/15)$, and (d) $Ru/B\text{-}ZrO_2(1/10)$ catalysts. The spectrum of the Ru foil is included as a reference.

the other hand, our result is inconsistent with that of Xie et al., who observed the monoclinic phase above 823 K [38]. The reason for their lower transformation temperature from tetragonal to monoclinic ZrO_2 may be due to the lacking of the digestion step for the amorphous zirconium oxyhydroxide. As pointed out by Chuah et al. [37], digesting the sample at 373 K for longer than 24 h is essential for obtaining a pure *t*-ZrO_2 that has high thermal stability. The B-ZrO_2 samples also presented the same *t*-ZrO_2 phase with no B-bearing diffractions being observed, which is anticipated due to the low amount of B doped in these samples (<3%, Table 1).

3.2. Acidic properties of the B-doped ZrO_2 samples

According to the literature [22], pyridine exhibited several vibration bands originating from different adsorption sites on *t*-ZrO_2 in room-temperature Py-IR spectrum; they are strong Lewis acid sites-coordinated pyridine (strong L-Py) at 1613 cm^{-1} (ν_{8a}), Lewis acid sites-coordinated pyridine (L-Py) at 1450 cm^{-1} (ν_{19b}), hydrogen-bonded pyridine (hb-Py) in the ranges of 1590–1600 and 1440–1447 cm^{-1} (ν_{8a} and ν_{19b}, respectively), and physically adsorbed pyridine (ph-Py) at 1581 and 1439 cm^{-1}. Both the ν_{8a} and ν_{19b} modes are the ring-breathing (ν_{CCN}) vibrations of pyridine [39]. All the bands decreased in intensity when elevating the desorption temperature. At 373 K, the bands arising from ph-Py and hb-Py were diminished, thus the remaining band at 1450 cm^{-1} could be unambiguously assigned to L-Py [22].

In light of that work, we collected the Py-IR spectra of the ZrO_2 and the B-ZrO_2 samples at 373 K, as displayed in Fig. 2. Consistent with previous finding [22], the ZrO_2 sample showed no band corresponding to the Brønsted acid sites at 1540 cm^{-1} [19], and only bands belonging to L-Py at 1606 and 1444 cm^{-1} were present. In the case of the B-ZrO_2 samples, it is interesting that new bands emerged at higher frequencies of 1626 and 1460 cm^{-1}, meanwhile the bands at 1606 and 1444 cm^{-1} were attenuated substantially. As far as we are aware of, there is no evidence for direct pyridine/B interaction in the literature from FTIR analysis.

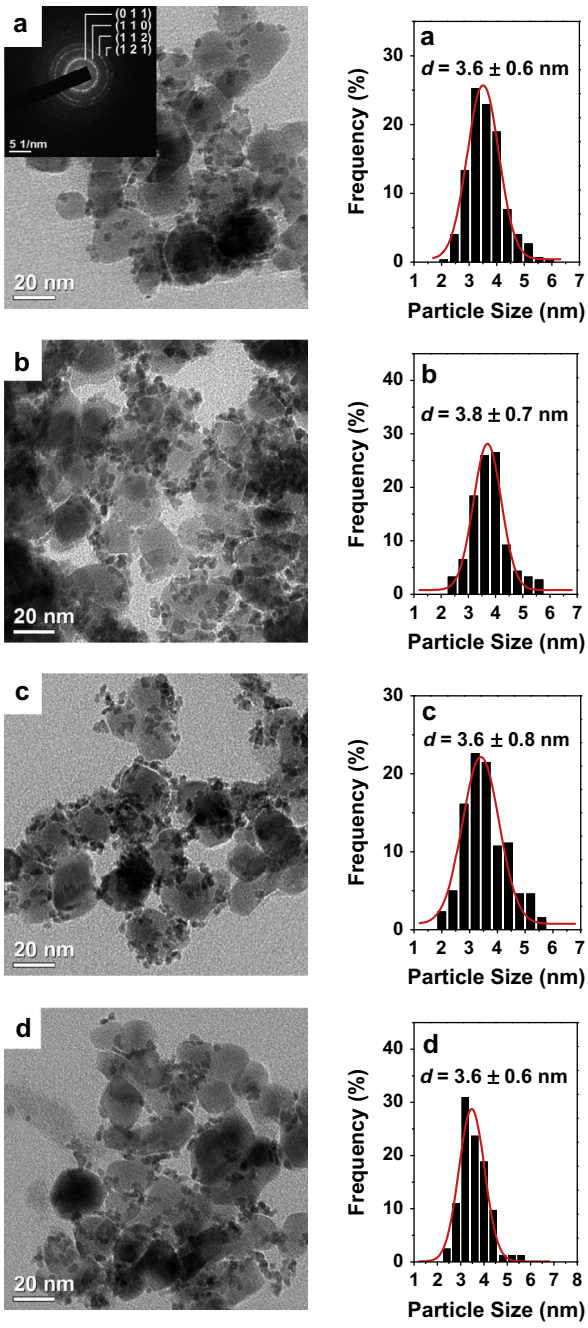

Fig. 6. TEM images and PSD histograms with Gaussian analysis fittings of the Ru NPs of the (a) Ru/ZrO_2, (b) $Ru/B\text{-}ZrO_2(1/20)$, (c) $Ru/B\text{-}ZrO_2(1/15)$, and (d) $Ru/B\text{-}ZrO_2(1/10)$ catalysts. Inset in (a) is the corresponding SAED pattern.

Moreover, considering the small amount of B doped in these B-ZrO_2 samples, it is logical to deduce that the new bands were not caused by pyridine coordinated directly on the B^{3+} sites. Rather, modification of the Lewis acid sites of ZrO_2 by B is a more plausible alternative. Chuah et al. found that after the impregnation of SiO_2 with 5 wt% B_2O_3, the bands at 1626 and 1462 cm^{-1} due to the coordinatively bonded pyridine at the Lewis acid sites became stronger [40]. They postulated that the Lewis acid sites were located at the Si atoms, because B^{3+} is very small in size, and its role as a Lewis acid site might be screened by the much bulkier O^{2-} ions. On the other hand, the electron-deficient B^{3+} could modify the Lewis acidity of Si via an inductive effect. A similar doping effect of B on the Lewis acidity of Zr^{4+} is expected for the B-ZrO_2 samples.

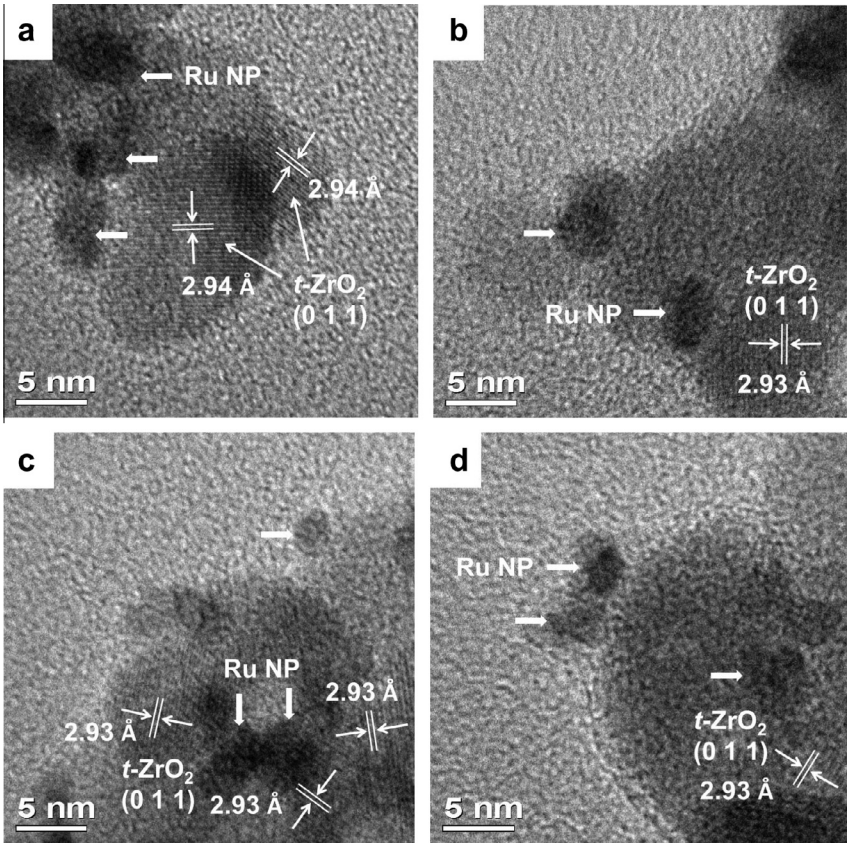

Fig. 7. HRTEM images of the (a) Ru/ZrO_2, (b) Ru/B-ZrO_2(1/20), (c) Ru/B-ZrO_2(1/15), and (d) Ru/B-ZrO_2(1/10) catalysts.

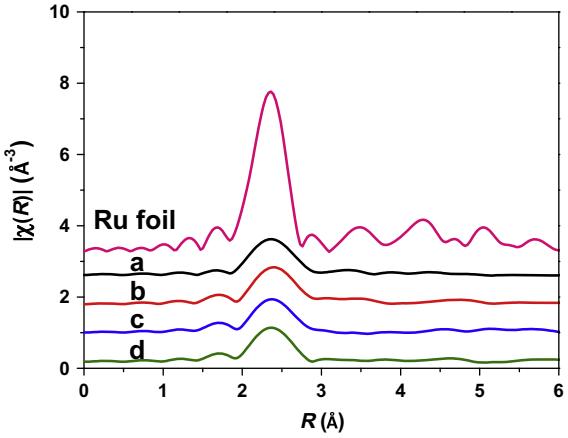

Fig. 8. The RDFs after Fourier transformation of the Ru K-edge k^2-weighted $\chi(k)$ data of the (a) Ru/ZrO_2, (b) Ru/B-ZrO_2(1/20), (c) Ru/B-ZrO_2(1/15), and (d) Ru/B-ZrO_2(1/10) catalysts. The RDF of the Ru foil is included as a reference.

According to Fig. 2, the amounts of the Lewis acid sites on the ZrO_2 and B-ZrO_2 samples were calculated from the total integral intensities of the bands at 1460 and 1444 cm^{-1}. Table 2 shows that the n_{Py} increased in the order of ZrO_2 < B-ZrO_2(1/20) < B-ZrO_2(1/15) < B-ZrO_2(1/10) with the improvement of the doping level of B. This order is consistent with the observation by Urbano et al. that the ZrO_2 samples modified with B had more Lewis acid sites [18].

Though pyridine is capable of discriminating and evaluating the Lewis acid and Brønsted acid sites, this molecule is relatively bulky and tends to underestimate the amount of the acid sites on porous materials. NH_3, with small dynamic diameter, can easily get access to the acid sites situated in small pores and, thus, was used to quantify the overall amount and strength of the acid sites. Fig. 3 shows the NH_3-TPD profiles of the ZrO_2 and the B-ZrO_2 samples. The ZrO_2 sample exhibited a broad peak at ~489 K attributable to NH_3 adsorbed on weak acid sites, and a shoulder peak at ~605 K and a small step at 700 K corresponding to NH_3 adsorbed on medium acid sites [41]. The B-ZrO_2 samples exhibited a similar three-peak profile, but the first two peaks shifted steadily to lower temperatures with the increment in the doping level of B, implying that B doping on ZrO_2 may lead to the formation of a new kind of Lewis acid sites not necessarily with enhanced acidity.

The overall acid amounts (n_{NH3}) on the ZrO_2 and B-ZrO_2 samples were determined by the integral peak areas under the NH_3 desorption curves. Table 2 shows that irrespective of the fact that the n_{NH3} is more than three times as high as the n_{Py} for each sample, the NH_3-TPD and Py-IR characterizations indicated the same sequence of the acid amount. The much lower acid amount derived from Py-IR is rationalized by the fact that pyridine is bulkier and less basic, as also reported by Góra-Marek et al. [42]. Both techniques involving different probe molecules agree with each other in the sense that the doping of B could increase the amount of the Lewis acid sites on ZrO_2. The n_{NH3} increased further on the B-ZrO_2(1/5) sample with the nominal B/Zr molar ratio of 1/5 (Fig. S2). As will be illustrated, the doping effect of B on the acidic properties of the B-ZrO_2 samples has important implications for the catalytic activity and selectivity of the Ru/B-ZrO_2 catalysts in the partial hydrogenation of benzene.

3.3. Chemical state and morphology of the Ru/B-ZrO_2 catalysts

With the as-synthesized B-doped ZrO_2 samples, we prepared the Ru/B-ZrO_2 catalysts by the wetness impregnation-chemical

Table 3
The structural parameters from the Ru K-edge EXAFS data of the Ru foil, and the Ru/ZrO_2 and $Ru/B\text{-}ZrO_2$ catalysts.

Sample	Pair	N	R (Å)	$\Delta\sigma^2$ (10^{-3} Å^2)	ΔE_0 (eV)
Ru foil	Ru–Ru	11.4 ± 1.0	2.68 ± 0.02	5.00	−3.8
Ru/ZrO_2	Ru–Ru	3.6 ± 0.4	2.74 ± 0.02	5.88	−0.6
	Ru–B	1.2 ± 0.1	2.46 ± 0.02	0.06	7.3
$Ru/B\text{-}ZrO_2(1/20)$	Ru–Ru	4.0 ± 0.4	2.70 ± 0.02	6.63	−1.3
	Ru–B	1.1 ± 0.1	2.45 ± 0.02	0.05	9.7
$Ru/B\text{-}ZrO_2(1/15)$	Ru–Ru	3.9 ± 0.4	2.70 ± 0.02	5.40	0.7
	Ru–B	0.9 ± 0.1	2.43 ± 0.02	0.06	16.6
$Ru/B\text{-}ZrO_2(1/10)$	Ru–Ru	4.2 ± 0.4	2.73 ± 0.02	5.97	−1.2
	Ru–B	1.0 ± 0.1	2.40 ± 0.02	0.09	5.2

reduction method. The compositional and textural properties of the Ru/ZrO_2 and $Ru/B\text{-}ZrO_2$ catalysts are compiled in Table S1. The catalysts had similar Ru loadings of about 7.3 wt% and bulk compositions of around $Ru_{91}B_9$, atomic ratio. They showed slightly lower S_{BET} and V_{pore} and slightly higher d_{pore} than those of the support counterparts due to the deposition of the metal. The dispersion of Ru and S_{Ru} is very similar for the catalysts (Table S1).

Fig. 4 shows the Ru 3p spectra of the Ru/ZrO_2 and $Ru/B\text{-}ZrO_2$ catalysts. The strongest Ru 3d peak was not employed to determine the chemical state of Ru for its partial overlapping with the C 1s peak of contaminant carbon. In Fig. 4, the Ru $3p_{3/2}$ BE of 462.1 eV and the $3p_{3/2}$–$3p_{1/2}$ doublet separation of 22.2 eV evidenced the metallic state of Ru in these catalysts [43]. This assignment is further validated by the Ru K-edge XANES spectra (Fig. 5), in which the Ru K-edge energies of the catalysts were identical to that of the Ru foil. Though the B 1s peak with low atomic sensitivity is unfortunately overlapped by the strong and broad signal from Zr [44], the identical Ru 3d and K-edge XANES energies between the Ru/ZrO_2 and $Ru/B\text{-}ZrO_2$ catalysts clearly demonstrate that there is no measurable electronic interaction between Ru and B in the supports.

Fig. 6 presents the TEM images and the PSD histograms with Gaussian analysis fittings of the Ru/ZrO_2 and $Ru/B\text{-}ZrO_2$ catalysts. In these figures, the Ru NPs verified by EDX displayed narrow PSDs in the range of 2–6 nm and mean sizes centered around 3.6 nm. The SAED pattern inset in Fig. 6a shows diffraction rings with spacings of 2.95, 2.53, 1.81, and 1.53 Å corresponding to the (0 1 1), (1 1 0), (1 1 2), and (1 2 1) planes of $t\text{-}ZrO_2$, respectively [45]. No extra diffraction ring or dot was resolved, which is in accordance with the amorphous structure of the Ru NPs prepared by the chemical reduction method [46].

3.4. Microstructure of the $Ru/B\text{-}ZrO_2$ catalysts

The high-resolution TEM (HRTEM) images in Fig. 7 show more structural details of the catalysts. Only the lattice fringes with the interplanar spacing of ~2.93 Å were visible for all four catalysts, which were ascribable to the (0 1 1) planes of $t\text{-}ZrO_2$. The shapes of the Ru NPs (marked by broad arrows) were approximately spherical. The Ru NPs on the four catalysts had similar size and were in close contact with the supports, which may be beneficial to the hydrogenation on the support by H_{so} from Ru discussed in the following section. No lattice fringe was observed on the Ru NPs in these HRTEM images because of their amorphous structure.

Considering that SAED and HRTEM described above as well as XRD cannot probe into the microstructure of the amorphous materials lacking of periodic atomic arrangement [2], we employed EXAFS to disclose the structural information of the amorphous Ru NPs. Fig. 8 shows the nonphase-corrected radial distribution functions (RDFs) transformed from the $k^2\chi(k)$ data of the Ru/ZrO_2 and $Ru/B\text{-}ZrO_2$ catalysts, with the Ru foil as a reference. It is acknowledged that the radial position of the Fourier transformed peak represents the distance between the absorbing atoms and their near neighbors. For the Ru foil with periodic atomic arrangement, aside from the strongest first nearest-neighbor peak at 2.36 Å, there were distinct second and third nearest-neighbor peaks at 3.48 and 4.29 Å, respectively. In contrast, only the first nearest-neighbor peak of the Ru atoms was obvious for the Ru/ZrO_2 and $Ru/B\text{-}ZrO_2$ catalysts, unambiguously confirming the short-range ordered but long-range disordered structure of the amorphous Ru NPs [2]. Moreover, the peak amplitudes of the catalysts were markedly lower than that of the Ru foil, characteristics of the reduced coordination number and the change in the phase from crystalline to amorphous. The virtually identical amplitudes of the Fourier transformed peaks for the four catalysts, however, signified their similar particle sizes [23], which is supportive of the TEM observations.

Table 3 summarizes the structural parameters extracted from the EXAFS data from the best fit for the Ru/ZrO_2 and $Ru/B\text{-}ZrO_2$ catalysts along with the Ru foil reference. The quality of the fitting is validated by the close resemblance of the simulated $k^2\chi(k)$ curves to the experimental data (Fig. S3). According to Table 3, the coordination number N and coordination distance R of the Ru/ZrO_2 catalyst were 3.6 and 2.74 Å for the Ru–Ru subshell and 1.2 and 2.46 Å for the Ru–B subshell, respectively. The Ru–B subshell is originated from the presence of a small amount of B in the Ru NPs (Table S1) prepared by the chemical reduction method [46]. Within the error ranges, there were no significant differences in the coordination number and interatomic distance for the Ru–Ru and Ru–B subshells between the Ru/ZrO_2 catalyst and the $Ru/B\text{-}ZrO_2$ catalysts. The experimental data were also fitted with both k^0 and k^1 weightings, with similar results being obtained.

3.5. Partial hydrogenation of benzene to cyclohexene

Fig. 9 illustrates the reaction courses of benzene hydrogenation over the Ru/ZrO_2 and $Ru/B\text{-}ZrO_2$ catalysts. The corresponding plots of the selectivity toward cyclohexene versus the conversion of benzene are shown in Fig. S4. Only the targeting intermediate cyclohexene and the complete hydrogenation product cyclohexane were detected as the products. No methyl cyclopentane was formed for the low reaction temperature. In Fig. 9, the contents of benzene decreased and cyclohexane increased monotonically throughout the reaction. As to the content of cyclohexene, there was a maximum at a certain reaction time dependent on the catalyst obeying the known behavior of the consecutive reaction. At extended reaction times, cyclohexene underwent further hydrogenation, and cyclohexane became the sole product.

Table 4 summarizes the catalytic results of the partial hydrogenation of benzene on the Ru/ZrO_2 and $Ru/B\text{-}ZrO_2$ catalysts. The r_0 values on the Ru/ZrO_2 and $Ru/B\text{-}ZrO_2$ catalysts are in the same order of magnitude with those of Hu and Chen [7] and Zhou

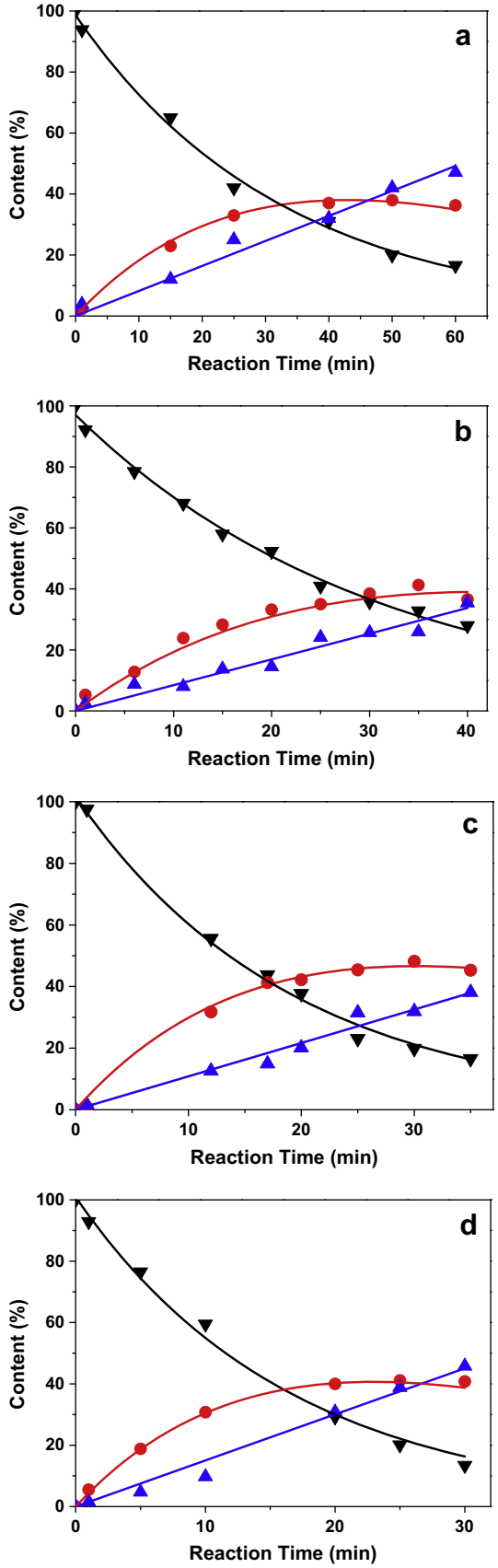

Fig. 9. The time courses of benzene hydrogenation over the (a) Ru/ZrO_2, (b) $Ru/B\text{-}ZrO_2(1/20)$, (c) $Ru/B\text{-}ZrO_2(1/15)$, and (d) $Ru/B\text{-}ZrO_2(1/10)$ catalysts. Reaction conditions: 1.0 g of catalyst, 100 ml of H_2O, 50 ml of benzene, 2.0 g of $ZnSO_4{\cdot}7H_2O$, temperature of 413 K, overall pressure of 4.0 MPa, and stirring rate of 1000 rpm. (▼) Benzene, (●) cyclohexene, and (▲) cyclohexane. Dots: experimental data; lines: fitted curves using the integrated rate equations developed in Ref. [6].

et al. [22]. It is further found that the r_0 was higher on the catalyst with higher doping level of B in ZrO_2. On the basis of the r_0 and the dispersion data, the TOFs of benzene over these catalysts were calculated, as listed in Table 4. The TOFs were higher than that on clay supported Ru catalyst (0.8 s^{-1}) [47]. It is identified that the TOFs increased moderately but steadily with the improvement of the doping level of B in ZrO_2.

In view of the similarities in the composition, particle size, chemical state, and geometric properties of the Ru NPs on the Ru/ZrO_2 and $Ru/B\text{-}ZrO_2$ catalysts verified above, the Ru NPs should not be responsible for the differences in the TOFs. Lin and Vannice found that the TOFs increased with the acid amounts on the supports of the supported Pt catalysts in benzene hydrogenation [15], attributable to additional hydrogenation of benzene on the acid sites of the support with H_{so}. According to Ishikawa et al. [48], the H_{so} species were also present on the support of the Ru/ZrO_2 catalyst. Their FT-IR study revealed that when H_2/D_2 was introduced to the Ru/ZrO_2 catalyst, H_2/D_2 dissociatively adsorbed on the Ru surface and spilled from Ru onto ZrO_2 to form the H_2O/D_2O-like species, which desorbed as H_2/D_2 but not as H_2O/D_2O. Following the approach raised by Ishikawa et al. [48], we acquired the DRIFTS spectra of adsorb hydrogen using the Ru/ZrO_2 and $Ru/B\text{-}ZrO_2(1/15)$ catalysts as representatives. In Fig. S5, a band at ~1608 cm^{-1} emerged at 323 K and increased in intensity when increasing the temperature to 413 K, which directly corroborates the formation of the H_{so} species [48].

On the other hand, as benzene with the delocalized π bonds is rich in electron, the electron-deficient Lewis acid site should be in favor of the adsorption of benzene. To prove the validity of this assumption, we examined the amount of benzene adsorbed on the Ru/ZrO_2 and $Ru/B\text{-}ZrO_2(1/15)$ catalysts by TPD. As displayed in Fig. 10, the desorption peak became stronger in the presence of the B dopant, which is consistent with the increase in the acid amount (Table 2), but incompatible with the change in the S_{BET} of the support (Table 1). On the $Ru/B\text{-}ZrO_2(1/5)$ catalyst, the intensity of the desorption peak increased further (Fig. S6). According to the kinetic study of the partial hydrogenation of benzene [6], the reaction on a ZrO_2-supported ternary Ru-based amorphous alloy catalyst under the conditions similar to the present case was first order with respect to benzene in the presence of water competing for the adsorption sites. To validate the first-order kinetics with respect to benzene on the $Ru/B\text{-}ZrO_2$ catalysts, a plot of the natural logarithm of benzene concentration against the reaction time derived from Fig. 9 was conducted, taking the $Ru/B\text{-}ZrO_2(1/15)$ catalyst as an example. As shown in Fig. S7, an excellent linear relationship was obtained, signifying that the reaction is first order with respect to benzene. Therefore, the higher the doping level of B in ZrO_2 is, the higher is the amount of benzene adsorbed on the acid sites reacting with H_{so} also adsorbed on the support, and, consequently, a higher TOF. By plotting the TOFs in Table 4 against the n_{NH3} values in Table 2, an excellent linear relationship emerged in Fig. 11a, which nicely substantiates the acid sites-mediated activity enhancement evoked by the doping of B in ZrO_2 for the $Ru/B\text{-}ZrO_2$ catalysts. Since the population of the medium-strength acid sites changed insignificantly with the improvement of the doping level of B (Fig. 2), the weak acid sites should dominate the changes in the catalytic performance on these catalysts.

3.6. Correlation of the acidic property with the selectivity toward cyclohexene

In many consecutive hydrogenation reactions, the product selectivity has been associated with the acidity of the support [49,50]. Scirè found that the selectivity to cyclohexanone decreased in the order of $Pd/La_2O_3 > Pd/CeO_2 > Pd/Al_2O_3$ in the selective hydrogenation of phenol, which was correlated with the

Table 4
The hydrogenation results of benzene on the Ru/ZrO_2 and $Ru/B\text{-}ZrO_2$ catalysts.[a]

Catalyst	Conv.[b] (%)	S_{CHE}[b] (%)	Y_{CHE}[b] (%)	t[b] (min)	S_0[c] (%)	$r_{0,BZ}$[d]	TOF (s^{-1})
Ru/ZrO_2	80	47	38	50	71	12.5	4.3
$Ru/B\text{-}ZrO_2(1/20)$	67	62	42	35	77	15.7	5.5
$Ru/B\text{-}ZrO_2(1/15)$	80	60	48	30	88	23.5	7.7
$Ru/B\text{-}ZrO_2(1/10)$	80	51	41	25	82	30.0	10.3

[a] Reaction conditions: 1.0 g of catalyst, 100 ml of H_2O, 50 ml of benzene, 2.0 g of $ZnSO_4{\cdot}7H_2O$, temperature of 413 K, overall pressure of 4.0 MPa, and stirring rate of 1000 rpm.
[b] Values recorded at the maximum yield of cyclohexene. S_{CHE} = selectivity toward cyclohexene; Y_{CHE} = yield of cyclohexene.
[c] Initial selectivity toward cyclohexene.
[d] Weight-specific activity, unit in mmol min^{-1} g_{cat}^{-1}.

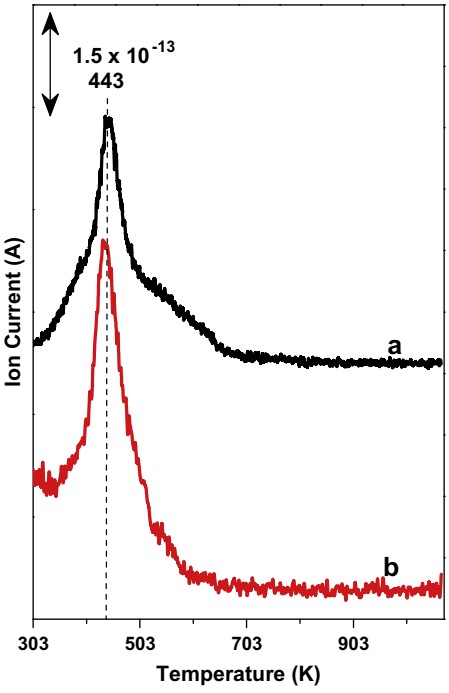

Fig. 10. TPD profiles of benzene on the (a) Ru/ZrO_2 and (b) $Ru/B\text{-}ZrO_2(1/15)$ catalysts.

reversed order of support acidity [49]. Ruta et al. found that for acetylene selective hydrogenation on the Pd/CNF/SMF catalysts, the selectivity to ethylene increased with the increase in the support acidity [50]. Analogously, as far as the close resemblance of the Ru NPs on the $Ru/B\text{-}ZrO_2$ catalysts is concerned, it is reasonable to assume that the differences in the selectivity toward cyclohexene is associated with the differences in the acidic properties of the supports.

As a result, in Fig. 11a the evolution of the S_0 against the n_{NH3} is also illustrated. Owing to the excellent linearity between selectivity and reaction time as exemplified in Fig. S8 using the reaction data of the $Ru/B\text{-}ZrO_2(1/15)$ catalyst, we directly extrapolated the fitted straight line of the selectivity–time curve of cyclohexene to zero reaction time to acquire S_0. Unlike the positive correlation of the TOF with the acid amount, a volcano-type relationship was established for the S_0, indicating that there is an optimal acid amount to maximize the selectivity toward cyclohexene on the $Ru/B\text{-}ZrO_2$ catalysts. The highest S_0 of 88% was obtained on the $Ru/B\text{-}ZrO_2(1/15)$ catalyst, which was higher than that on the Ru/La_2O_3–ZnO catalyst (80%) [7]. As the selectivity toward cyclohexene is determined by the relative hydrogenation rates of the benzene to cyclohexene step and the cyclohexene to cyclohexane step as schematically illustrated in Fig. 11b, by fitting the reaction

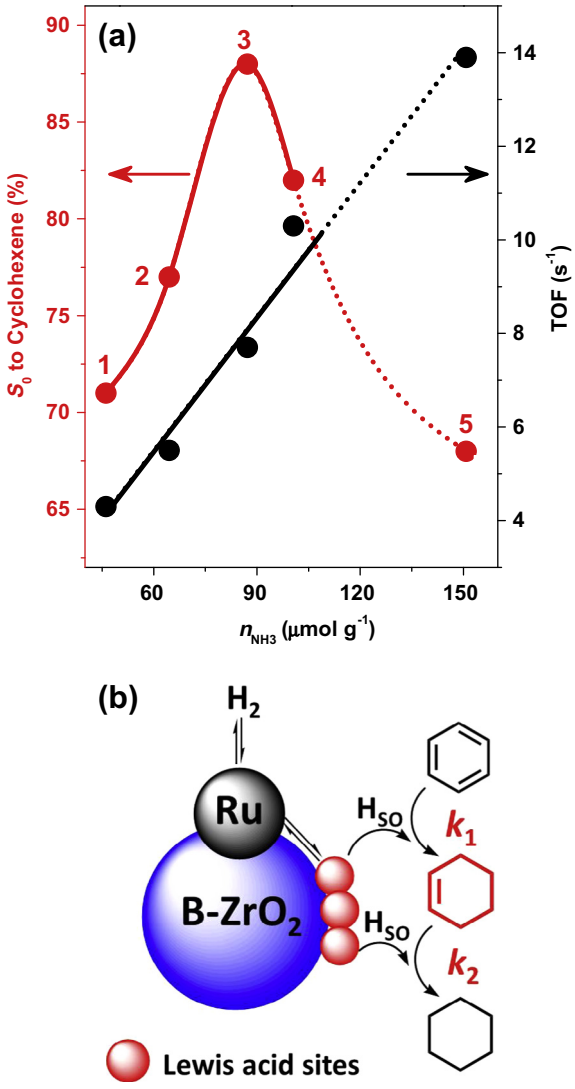

Fig. 11. (a) Correlations of TOF and S_0 with n_{NH3} on the supports of the (1) Ru/ZrO_2, (2) $Ru/B\text{-}ZrO_2(1/20)$, (3) $Ru/B\text{-}ZrO_2(1/15)$, (4) $Ru/B\text{-}ZrO_2(1/10)$, and (5) $Ru/B\text{-}ZrO_2(1/5)$ catalysts. (b) A schematic illustration of the mechanism for benzene hydrogenation on the acid sites of the Ru/ZrO_2 and $Ru/B\text{-}ZrO_2$ catalysts with H_{so}.

data presented in Fig. 9 using the integrated rate equations developed by Liu and coworkers [6], we obtained the rate constants k_1 and k_2 for these two steps. It turns out that by elevating the doping level of B, the k_1 and k_2 values increased concurrently, but the extents of the increments were not the same. As listed in Table 5, the evolution of the k_1/k_2 ratio mimicked that of the S_0, implying that the acid sites on the supports took effect on the selectivity toward cyclohexene by modifying the hydrogenation rates of both

Table 5
The rate constants for the hydrogenation of benzene to cyclohexene (k_1) and cyclohexene to cyclohexane (k_2) over the Ru/ZrO_2 and Ru/B-ZrO_2 catalysts fitted from reaction data in Fig. 9 according to the kinetic equations raised by Ref. [6].

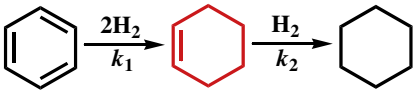

Catalyst	k_1 (10^{-2} min^{-1})	k_2 (10^{-2} mol l^{-1} min^{-1})	k_1/k_2 (10^{-2} l mol^{-1})
Ru/ZrO_2	3.0	82	3.7
Ru/B-ZrO_2(1/20)	3.3	84	3.9
Ru/B-ZrO_2(1/15)	5.2	108	4.8
Ru/B-ZrO_2(1/10)	6.1	150	4.1

benzene and cyclohexene. The hydrogenation of cyclohexene under the same conditions except for replacing benzene by the same volume of cyclohexene was also performed. The TOFs of cyclohexene over the Ru/ZrO_2, Ru/B-ZrO_2(1/20), Ru/B-ZrO_2(1/15), and Ru/B-ZrO_2(1/10) catalysts were 9.6, 11.5, 14.8, and 21.1 s^{-1}, respectively, which supports the above argument and is consistent with the findings of Appay et al. [51] and Aboul-Gheit et al. [52,53]. We found that the volcanic S_0–acid site relationship demonstrated in Fig. 11a is also held when using the n_{Py} derived from the Py-IR spectra in place of the n_{NH3} determined by NH_3-TPD. Moreover, when the nominal B/Zr molar ratio was improved to 1/5, the TOF and the S_0 values acquired on the Ru/B-ZrO_2(1/5) catalyst still adhered to the straight line and the volcanic curve, respectively, which manifests the crucial role of the support acidity on the catalytic performance of the Ru/B-ZrO_2 catalysts in the partial hydrogenation of benzene to cyclohexene.

In addition, the stability of the Ru/B-ZrO_2 catalysts was examined using the Ru/B-ZrO_2(1/15) catalyst as a representative. After each catalytic run, the organic phase was removed by suction, and the residual aqueous mixture containing the catalyst and $ZnSO_4$ was reused in a successive run without further catalyst reactivation. It is found that the benzene conversion at the same time span decreased only by 10% after three successive runs, possibly due to inevitable catalyst loss during sampling the reaction mixture at intervals for product analysis. Meanwhile, the conversion–selectivity curves were virtually identical among different runs, indicating that the nature of the catalyst did not change. After reaction, the aqueous phase was filtrated for chemical analysis. The Ru content was found to be below the detection limit (<0.17 ppb), showing that the leaching of Ru was negligible.

4. Conclusions

The B-doped ZrO_2 samples with the same t-ZrO_2 crystallographic form but different amounts of the Lewis acid sites were synthesized by adjusting the B/Zr ratios. The Ru NPs supported on these B-ZrO_2 samples exhibited similar size, chemical state, and microstructure, possibly due to the relatively low loading of Ru on the supports. In the partial hydrogenation of benzene to cyclohexene, the TOF of benzene linearly correlated with the amount of the Lewis acid sites, while the S_0 of cyclohexene exhibited a volcanic-type evolution, passing through the highest S_0 of 88% and the maximum yield of cyclohexene of 48% on the Ru/B-ZrO_2(1/15) catalyst. It is found that the Lewis acid sites on the supports operated in the reaction by altering the hydrogenation rates of the benzene to cyclohexene step and the cyclohexene to cyclohexane step. The acidity–performance relationship presented by this work paves the way for developing more efficient catalyst in the partial hydrogenation of benzene by engineering the acidic properties of the supports. As a result, investigations of the effects of the sources of Zr and B as well as dopants other than B on the partial hydrogenation of benzene are currently being carried out.

Acknowledgments

This work was supported by the National Basic Research Program of China (2012CB224804), the National Science Foundation of China (21073043, 21373055), the Science and Technology Commission of Shanghai Municipality (08DZ2270500), the Shanghai Synchrotron Radiation Facility, and the SINOPEC (S411063).

Appendix A. Supplementary material

Supplementary data associated with this article can be found, in the online version, at http://dx.doi.org/10.1016/j.jcat.2013.12.022.

References

[1] E. Dietzsch, U. Rymsa, D. Hönicke, Chem. Eng. Technol. 22 (1999) 130–133.
[2] Y. Pei, G.B. Zhou, N. Luan, B.N. Zong, M.H. Qiao, F. Tao, Chem. Soc. Rev. 41 (2012) 8140–8162.
[3] P. Zhang, T.B. Wu, T. Jiang, W.T. Wang, H.Z. Liu, H.L. Fan, Z.F. Zhang, B.X. Han, Green Chem. 15 (2013) 152–159.
[4] F. Schwab, M. Lucas, P. Claus, Angew. Chem. Int. Ed. 50 (2011) 10453–10456.
[5] G.Y. Fan, R.X. Li, X.J. Li, H. Chen, Catal. Commun. 9 (2008) 1394–1397.
[6] S.C. Liu, Y.Q. Guo, X.L. Yang, Y.L. Ji, G. Luo, Chin. J. Catal. 24 (2003) 42–46.
[7] S.C. Hu, Y.W. Chen, Ind. Eng. Chem. Res. 36 (1997) 5153–5159.
[8] H. Nagahara, M. Ono, M. Konishi, Y. Fukuoka, Appl. Surf. Sci. 121 (122) (1997) 448–451.
[9] G.C. Bond, Catalysis by Minerals, Academic Press, New York, 1962.
[10] A. Stanislaus, B.H. Cooper, Catal. Rev. Sci. Eng. 36 (1994) 75–123.
[11] A. de Mallman, D. Barthomeuf, J. Chim. Phys. 87 (1990) 535–538.
[12] J. Wang, L.M. Huang, H.Y. Chen, Q.Z. Li, Catal. Lett. 55 (1998) 157–163.
[13] L.J. Simon, J.G. van Ommen, A. Jentys, J.A. Lercher, Catal. Today 73 (2002) 105–112.
[14] J. Wang, H.Y. Chen, Q.Z. Li, React. Kinet. Catal. Lett. 69 (2000) 277–284.
[15] S.D. Lin, M.A. Vannice, J. Catal. 143 (1993) 539–553.
[16] Z.Y. Liu, H.J. Sun, D.B. Wang, W. Guo, X.L. Zhou, S.C. Liu, Z.J. Li, Chin. J. Catal. 31 (2010) 150–152.
[17] Z.Y. Liu, H.J. Sun, D.B. Wang, S.C. Liu, Z.J. Li, Chin. J. Chem. 28 (2010) 1927–1934.
[18] F.J. Urbano, M.A. Aramendía, A. Marinas, J.M. Marinas, J. Catal. 268 (2009) 79–88.
[19] T.R. Hughes, H.M. White, J. Phys. Chem. 71 (1967) 2192–2201.
[20] T. Onfroy, G. Clet, M. Houalla, Micropor. Mesopor. Mater. 82 (2005) 99–104.
[21] A. Travert, A. Vimont, J.C. Lavalley, V. Montouillout, M.R. Delgado, J.J.C. Pascual, C.O. Areán, J. Phys. Chem. B 108 (2004) 16499–16507.
[22] G.B. Zhou, J.L. Liu, X.H. Tan, Y. Pei, M.H. Qiao, K.N. Fan, B.N. Zong, Ind. Eng. Chem. Res. 51 (2012) 12205–12213.
[23] A.M. Karim, V. Prasad, G. Mpourmpakis, W.W. Lonergan, A.I. Frenkel, J.G. Chen, D.G. Vlachos, J. Am. Chem. Soc. 131 (2009) 12230–12239.
[24] C.H. Bartholomew, R.J. Farrauto, Fundamentals of Industrial Catalytic Processes, second ed., John Wiley & Sons Inc., Hoboken, New Jersey, 2006. pp. 147–148.
[25] B.J. Hwang, L.S. Sarma, J.M. Chen, C.H. Chen, S.C. Shih, G.R. Wang, D.G. Liu, J.F. Lee, M.T. Tang, J. Am. Chem. Soc. 127 (2005) 11140–11145.
[26] B. Ravel, M. Newville, J. Synchrotron Rad. 12 (2005) 537–541.
[27] J.S. Gao, A. Yang, Y.J. Chen, J.P. Kirkland, J. Lou, N.X. Sun, C. Vittoria, V.G. Harris, J. Appl. Phys. 105 (2009). 07A323-1–07A323-3.
[28] H.J. Sun, S.H. Li, Y.X. Zhang, H.B. Jiang, L.L. Qu, S.C. Liu, Z.Y. Liu, Chin. J. Catal. 34 (2013) 1482–1488.
[29] J.Q. Wang, Y.Z. Wang, S.H. Xie, M.H. Qiao, H.X. Li, K.N. Fan, Appl. Catal. A 272 (2004) 29–36.
[30] J. Struijk, M. d'Angremond, W.J.M. Lucas-de Regt, J.J.F. Scholten, Appl. Catal. A 83 (1992) 263–295.
[31] H.J. Sun, C. Zhang, P. Yuan, J.X. Li, S.C. Liu, Chin. J. Catal. 29 (2008) 441–446.
[32] H. Wang, Z.Y. Liu, R.J. Shi, Y.N. Zhang, H.Q. Zhang, S.C. Liu, Chin. J. Catal. 26 (2005) 407–411.
[33] M. Hronec, Z. Cvengrošová, M. Králik, G. Palma, B. Corain, J. Mol. Catal. A 105 (1996) 25–30.
[34] H.J. Sun, H.B. Jiang, S.H. Li, Y.Y. Dong, H.X. Wang, Y.J. Pan, S.C. Liu, M.S. Tang, Z.Y. Liu, Chem. Eng. J. 218 (2013) 415–424.
[35] R.S. Suppino, R. Landers, A.J.G. Cobo, Appl. Catal. A 452 (2013) 9–16.
[36] M. Boudart, Chem. Rev. 95 (1995) 661–666.
[37] G.K. Chuah, S. Jaenicke, S.A. Cheong, K.S. Chan, Appl. Catal. A 145 (1996) 267–284.
[38] S.B. Xie, E. Iglesia, A.T. Bell, Chem. Mater. 12 (2000) 2442–2447.

[39] G.A.H. Mekhemer, S.A. Halawy, M.A. Mohamed, M.I. Zaki, J. Phys. Chem. B 108 (2004) 13379–13386.
[40] D.B. Ravindra, Y.T. Nie, S. Jaenicke, G.K. Chuah, Catal. Today 96 (2004) 147–153.
[41] W.H. Chen, H.H. Ko, A. Sakthivel, S.J. Huang, S.H. Liu, A.Y. Lo, T.C. Tsai, S.B. Liu, Catal. Today 116 (2006) 111–120.
[42] K. Góra-Marek, J. Datka, S. Dzwigaj, M. Che, J. Phys. Chem. B 110 (2006) 6763–6767.
[43] J.F. Moulder, W.F. Stickle, P.E. Sobol, K.D. Bomben, Handbook of X-ray Photoelectron Spectroscopy, in: J. Chastain (Ed.), Perkin-Elmer, Eden Prairie, Minnesota, 1992, p. 242.
[44] S.C. Liu, Z.Y. Liu, Z. Wang, S.H. Zhao, Y.M. Wu, Appl. Catal. A 313 (2006) 49–57.
[45] J. Málek, L. Beneš, T. Mitsuhashi, Powder Diffr. 12 (1997) 96–98.
[46] S.H. Xie, M.H. Qiao, H.X. Li, W.J. Wang, J.F. Deng, Appl. Catal. A 176 (1999) 129–134.
[47] O.B. Shawkataly, R. Jothiramalingam, F. Adam, T. Radhika, T.M. Tsao, M.K. Wang, Catal. Sci. Technol. 2 (2012) 538–546.
[48] H. Ishikawa, J.N. Kondo, K. Domen, J. Phys. Chem. B 103 (1999) 3229–3234.
[49] S. Scirè, S. Minicò, C. Crisafulli, Appl. Catal. A 235 (2002) 21–31.
[50] M. Ruta, N. Semagina, L. Kiwi-Minsker, J. Phys. Chem. C 112 (2008) 13635–13641.
[51] M.D. Appay, J.M. Manoli, C. Potvin, M. Muhler, U. Wild, O. Pozdnyakova, Z. Paál, J. Catal. 222 (2004) 419–428.
[52] A.K. Aboul-Gheit, S.M. Aboul-Fotouh, S.M. Abdel-Hamid, N.A.K. Aboul-Gheit, J. Mol. Catal. A 245 (2006) 167–177.
[53] A.K. Aboul-Gheit, N.A.K. Aboul-Gheit, Appl. Catal. A 303 (2006) 141–151.